



Design of 10 MeV electron linear accelerator for space environment simulation

Shu Zhang^{1,2} · Cai Meng^{1,2} · Zu-Sheng Zhou^{1,2} · Xiang He¹ · Jing-Ru Zhang¹ · Munawar Iqbal¹ · Zhan-Dong Zhang¹ · Bo-Wen Bai³ · Yun-Long Chi¹

Received: 22 November 2023 / Revised: 22 January 2024 / Accepted: 10 February 2024 / Published online: 25 September 2024
© The Author(s), under exclusive licence to China Science Publishing & Media Ltd. (Science Press), Shanghai Institute of Applied Physics, the Chinese Academy of Sciences, Chinese Nuclear Society 2024

Abstract

A compact 10 MeV S-band irradiation electron linear accelerator (linac) was developed to simulate electronic radiation in outer space and perform electron irradiation effect tests on spacecraft materials and devices. According to the requirements of space environment simulation, the electron beam energy can be adjusted in the range from 3.5 to 10 MeV, and the average current can be adjusted in the range from 0.1 to 1 mA. The linac should be capable of providing beam irradiation over a large area of 1 m² with a uniformity greater than 90% and a scanning rate of 100 Hz. A novel method was applied to achieve such a high beam scanning rate by combining a kicker and a scanning magnet. Based on this requirement, a design for the 10 MeV linac is proposed with an RF power pulse repetition rate of 500 Hz; it includes a thermal cathode electron gun, a bunching-accelerating section, and a scanning transport line. The detailed physical design and dynamic simulation results of the proposed 10 MeV electron linac are presented in this paper.

Keywords Electron linac · Accelerating structure · Beam scanning · Beam homogenization · Irradiation linac

1 Introduction

Electron linacs are important particle accelerators. Large scientific facilities use injectors for circular accelerators, linear colliders, and free-electron lasers. As functional devices, electron linacs have attracted wide attention [1] and have been applied in various sectors of the national economy, such as food irradiation sterilization, preservation, and degradation of chemical pollutants [2], radiation processing in industry, customs probing, medical treatment, disinfection, and sterilization of medical instruments [3]. In addition, linacs have important applications in the study of radiation

effects on spacecraft. A great deal of electrons and protons exist in space. High-energy electrons are trapped by the Earth's magnetic field and form Van Allen radiation belts, in which the energy of electrons can reach 10 MeV [4]. The radiation of these high-energy charged particles leads to the aging of materials, devices, and system-level components used in spacecraft, thereby affecting their reliability. The aerospace industry is an important area of international competition, and the development of a strong aerospace sector is a major national strategic goal. An increasing number of spacecraft will enter space in the future. Therefore, there is an urgent need for conducting research on the behavioral evolution of spacecraft materials, devices, and system-level components under the effect of high-energy electron irradiation to build a database for spacecraft reliability design and lifetime prediction. In this context, the construction of a large-scale space science and technology experimentation platform, the Space Environment Simulation and Research Infrastructure (SESRI), was proposed. In this platform, the electronic environment of extraterrestrial space can be simulated in terms of radiation tolerance using an electron linac.

A 10 MeV electron linear accelerator is an important component of the integrated environmental simulation

✉ Cai Meng
mengc@ihep.ac.cn

✉ Yun-Long Chi
chiyl@ihep.ac.cn

¹ Institute of High Energy Physics, Chinese Academy of Sciences, Beijing 100049, China

² University of Chinese Academy of Sciences, Beijing 100049, China

³ Institute of Special Environments Physical Sciences, Harbin Institute of Technology, Shenzhen 518055, China

system of the SESRI. It provides a ground research platform for conducting high-energy irradiation experiments, studying the behavior of irradiation damage, and revealing its physical mechanisms [5]. The electron linac for space environment simulation proposed in this paper has stringent requirements and can provide an electron beam with a wide spatial range of scanning capability, reaching energy levels of 10 MeV and an average current of 1 mA. The main specifications of the 10 MeV linac listed in Table 1 are challenging in terms of design and operation. In particular, the scanning rate, along with a large scanning area and high uniformity, is relevant features of irradiation electron linacs worldwide [5–7]. To meet the design requirement of 100 Hz beam scanning rate, a novel method was applied that makes use of a scanning magnet (SM) for vertical scanning and a kicker for horizontal scanning. According to the aforementioned main specifications and an investigation of the relevant literature, the design considerations of the proposed linac are first outlined. Subsequently, the detailed physical design and dynamic simulation results for the electron gun, accelerating structure, and scanning transport line are presented. Finally, hardware considerations and preliminary linac commissioning are discussed.

2 Design parameters of 10 MeV electron linac

To satisfy the main specifications and consider the size of the site and floor area of the accelerator equipment, we followed the principles of structural simplicity and implementation feasibility to design the overall structure of the accelerator. The design parameters of the linac are presented and discussed in the following sections.

2.1 Accelerator repetition rate

The application of beam irradiation typically requires the creation of a uniformly distributed area on a target.

Table 1 Main specifications of the 10 MeV linac

Parameter	Value
Accelerator length, L_a (m)	≤ 10
Beam energy, W_0 (MeV)	3.5–10
Average beam current, I_{ave} (mA)	0.01–1
Energy spread, δ (%)	≤ 6 (3.5 MeV) ≤ 2.5 (10 MeV)
Emittance, ε (mm · mrad)	≤ 30 (10 MeV)
Irradiation area, A_s (m ²)	0.2×0.2 (Target A) 1×1 (Target B)
Beam intensity uniformity, S (%)	≥ 90

Commonly used methods for beam homogenization include scatterer homogenization [8], distribution transformation using multipole magnets, and scanning magnets [9]. In the scatterer homogenization method, electrons in the beam collide with those in the scattering material, resulting in significant beam loss, making it unsuitable for high-power conditions. The transformation method uses the nonlinear force of multipole magnets to redistribute the beam phase space, thereby establishing a relatively uniform irradiated area after a specific transport period. The nonlinear magnets used in this method include sextupole [10], octupole [11], dodecapole [12], step-like [13], and iron pole-piece nonlinear magnets [14]. However, the higher-order nonlinear terms of the magnets cause coupling in the transverse direction, which requires a longer transport line to eliminate the coupling and more complex elements to match the beam. Because a linac has a length limitation, the transformation method is difficult to apply. The method based on SMs uses mutually orthogonal time-varying deflecting magnetic fields in both transverse beam directions. After the beam completes the scan in one direction, the magnetic field in the other direction increases in one step and finally forms a two-dimensional uniform distribution on the target. When the distance between adjacent pulsed beam spots d_e is equal to the beam spot diameter φ_e (FWHM), the scanning becomes most uniform and continuous [15]. The one-dimensional magnet scanning rate N_m must satisfy the expression

$$\frac{N_m}{f} \geq \frac{W_e}{\varphi_e} + 1, \quad (1)$$

where f is the scanning rate, and W_e is the width of the irradiated area. The repetition rate of the linac is the product of the scanning frequency of the magnets in both directions.

The 100 Hz scanning rate of this linac is much higher than that of conventional irradiation accelerators. According to Eq. (1), to achieve a beam spot of 0.04 m² (or 1 m²) with more than 90% uniformity using the conventional SM method, the product of the scanning rate in both directions must exceed thousands of Hz. This requires a high repetition rate superconducting accelerator, which is extremely expensive. Therefore, based on a normal conducting linear accelerator, we propose a scanning method in which an SM is replaced by a kicker that generates a linearly varying electromagnetic field within a few tens of microseconds in the horizontal direction to complete fast scanning within a beam pulse [16] and achieve a uniform distribution. A vertical SM is used to apply different magnetic field strengths to each macrobeam pulse, which deflects the beam to a different position. Subsequently, multiple pulsed beams are superimposed to form a uniform distribution within a certain range in the vertical direction. A Gaussian distribution given by Eq. (2) is used as the beam distribution to model the superposition of the pulsed beams in the vertical

direction, as shown in Fig. 1. In this context, μ represents the deflection distance of the pulsed beam in the y -direction, and σ denotes the beam size. The final distribution in the y -direction is obtained by superimposing several beams, which is denoted as ‘beam pulse total’ in Fig. 1.

$$f(y) = \frac{1}{\sqrt{2\pi}\sigma} e^{-\left(\frac{y-\mu}{2\sigma}\right)^2} \tag{2}$$

The regions on the target are divided into equal intervals, the beam intensity in each region is measured, and the beam intensity uniformity is calculated using the following equations:

$$S_x = \sqrt{\frac{\sum_{i=1}^n (x_i - \bar{x}_n)^2}{n - 1}}, \tag{3}$$

$$S = \left(1 - \frac{S_x}{\bar{x}_n}\right) \times 100\%, \tag{4}$$

where n is the number of regions, x_i is the beam intensity in a region, \bar{x}_n is the average beam intensity on the target, S_x is the standard deviation of the beam intensity, and S represents the beam intensity uniformity. The beam percentage is defined as the ratio of the number of particles on the target to the total number of particles.

The accelerator repetition rate N is determined by the scanning rate and number of scan magnet steps T in each scanning period as follows:

$$N = fT. \tag{5}$$

Increasing the beam size can improve the beam intensity uniformity; however, it decreases the beam percentage.

Likewise, increasing the number of scanning steps can improve the uniformity of the irradiated area; however, it increases the repetition rate of the linac. Figure 2 shows the relationship between beam percentage and uniformity under the superposition of different numbers of pulsed beams within the 0.2 m range. An appropriate beam size is used for each case. To improve the irradiation efficiency, the beam percentage should be as high as possible. When the beam percentage exceeds 60%, only five or more pulsed beams can form a distribution with uniformity higher than 90% within 0.2 m. Six pulsed beams can achieve a distribution with higher uniformity; however, this increases the repetition rate. Taking all these factors into account, five superimposed pulsed beams were finally adopted. Therefore, the repetition rate of the linac is 500 Hz. This scheme requires a small horizontal beam size and a large vertical beam size, which reduces the design difficulty of the transport line.

2.2 Beam pulse current

The average beam current I_{avg} is calculated using the pulse current i_b , beam pulse width t , and repetition rate as follows:

$$I_{avg} = i_b t N. \tag{6}$$

The maximum average power that a ceramic window can withstand at the klystron output is 40 kW. The maximum microwave pulse width at 5 MW RF peak power and 500 Hz repetition rate is 16 μ s. Considering the filling time of the accelerating structure, the beam pulse width t should not exceed 15 μ s. A short RF pulse implies a high pulse current, which results in a stronger beam loading effect [17, 18], thereby reducing the energy gain. Taking all these factors into account, we selected a beam pulse width of 15 μ s. According to the maximum average beam current of 1 mA,

Fig. 1 (Color online) Schematic of beam pulse superposition. The horizontal coordinate indicates the position of the beam in the y -direction, whereas the vertical coordinate indicates the normalized particle density

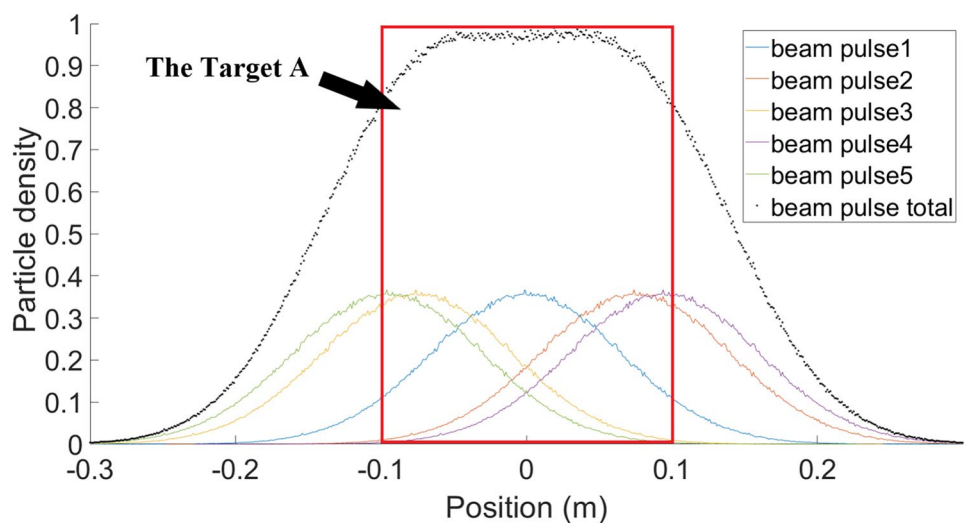
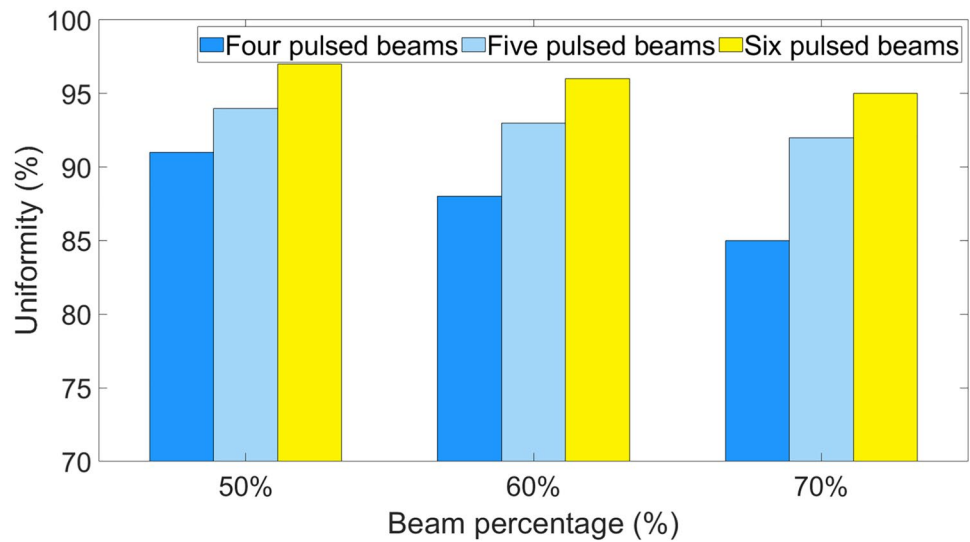


Fig. 2 (Color online) Relationship between beam percentage and uniformity under the superposition of different numbers of pulsed beam within 0.2 m



the maximum pulse current is calculated to be 133.3 mA. For irradiation accelerators, assuming a transmission efficiency of approximately 70%, the electron gun needs to emit a pulsed beam with an adjustable current ranging from 2 to 200 mA.

2.3 Layout design

To accommodate the limitations of the equipment site and simplify the accelerator design, a conventional bunching system scheme is proposed in which a pre-buncher (PB) provides the initial bunching. According to this requirement, the beam energy is continuously adjusted from 3.5 to 10 MeV. A two-stage accelerating scheme is proposed to minimize the phase slip of the beam in the accelerating structure of the low-energy section and ensure the stability of the accelerating process while flexibly controlling the exit energy. The first stage of the accelerating structure

bunches and accelerates. Thus, the beam is accelerated to approximately 6.75 MeV. The second stage of the accelerating structure adjusts the beam energy from 3.5 to 10 MeV by adjusting the RF phase to achieve acceleration or deceleration. To reduce the voltage requirements of the electron gun and improve the bunching efficiency, a variable phase velocity (β_ϕ) cavity is initially adopted for the accelerating structure. The 10 MeV electron linac is mainly composed of a thermionic cathode electron gun, bunching-accelerating section, and scanning transport line. The layout is shown in Fig. 3.

An energy analysis station was introduced into the transport line to measure the beam energy and energy spread, as well as to monitor the energy stability. The beam distribution is obtained using a beam profile monitor (PR). A beam position monitor (BPM) is used to monitor the beam orbit and energy stability. The varying quadrupole magnet strength method [19] is used to measure the beam emittance.

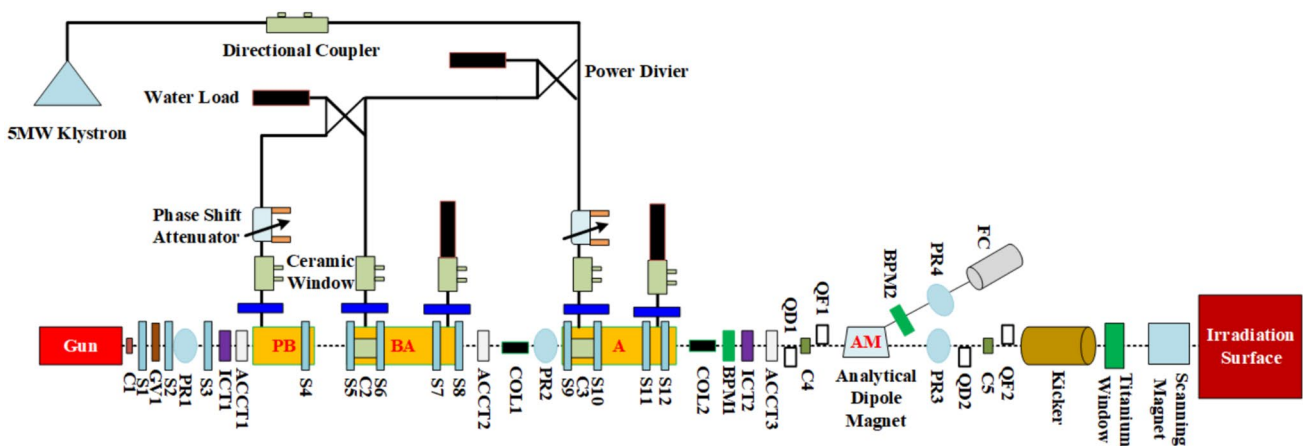


Fig. 3 (Color online) Layout of 10 MeV electron linac

A kicker and an SM are used to perform beam scanning in the horizontal and vertical directions, respectively. Four quadrupole magnets are used for beam size matching to meet the requirements of beam intensity uniformity. A Faraday cup (FC) array was placed on Targets A and B to measure the beam intensity uniformity.

3 Physical design of 10 MeV electron linac

3.1 Thermal cathode electron gun

As the source of the accelerator, the design of the electron gun mainly considers two aspects: emission current and beam quality. Considering current adjustability, a grid-controlled electron gun is used, with an extra grid between the cathode and anode. The emission current is controlled by varying the grid voltage. Considering the beam quality, the transverse emittance should be small to improve the transmission efficiency. The EGUN program [20] was used to simulate the electron gun at a high voltage of 60 kV. The design and optimization of the electron gun were conducted at a current intensity of 200 mA. The simulation results for 2 mA are presented in Table 2.

3.2 Bunching-accelerating section

The bunching-accelerating section consists of a PB, a bunching-accelerating (BA) structure, and an accelerating structure (AS), which are driven by a 5 MW klystron. Power dividers [21] and waveguide phase shift attenuators are used to distribute the RF power and adjust the phase. To save space and improve the transmission efficiency, solenoids are used to control the transverse envelope of the beam.

3.2.1 Pre-buncher

To improve the bunching efficiency, we propose a PB to initially compress the beam at the exit of the electron gun, allowing as many subsequent particles as possible to be captured and accelerated by the accelerating structure. The PB is a window-coupled standing-wave cavity designed at a resonant frequency of 2856 MHz. Window coupling can

withstand a high peak power and is less susceptible to sparking, thereby improving the stability of the PB operation [22]. The design parameters are presented in Table 3.

In contrast with the accelerating electric field established by the RF power flowing from the input to the output of the traveling-wave cavity, the accelerating electric field of the standing-wave cavity is generated by the RF power reflected back and forth in the cavity. When there is no load in the cavity, the power in the cavity P_c is described by the following relationship with the input power P_{in} :

$$P_c = \frac{4\beta_c}{(1 + \beta_c)^2} P_{in}. \tag{7}$$

According to the definition of shunt impedance,

$$Z_s = \frac{E_{sw}^2}{P_w}, \tag{8}$$

where E_{sw} is the accelerating gradient, P_w is the power loss per unit length in the cavity, and $P_w = P/L$, where L is the cavity length.

According to Eqs. (7) and (8), the accelerating gradient of the standing-wave cavity is given by

$$E_{sw} = \frac{2\sqrt{\beta_c}}{1 + \beta_c} \sqrt{\frac{Z_s P_{in}}{L}}. \tag{9}$$

When passing through the cavity, the charged particles induce an electric field in the direction opposite to that of the accelerating electric field, and the magnitude is proportional to the charge. At this point, the accelerating electric field in the cavity is significantly smaller than when there is no beam. This effect is known as beam loading. Equation (9) describes the relationship between the accelerating gradient and the power when no beam enters the cavity. When the beam passes through, part of the power in the cavity is acquired by the beam, and the accelerating gradient E_c in the cavity is expressed as follows [23–25]:

$$E_c = \frac{2\sqrt{\beta_c}}{1 + \beta_c} \sqrt{\frac{Z_s P_{in}}{L}} - \frac{Z_s}{1 + \beta_c} I_b. \tag{10}$$

For the proposed design, the accelerating gradient E_c in the cavity is 0.26 MV/m. Considering the strongest beam

Table 2 Parameters of electron gun

Parameter	Mode1	Mode2
Beam energy, W_0 (keV)	60	60
Pulse current, i_b (mA)	200	2
Pulse width, t (μ s)	15	15
Emittance, ϵ (mm · mrad)	4.1	4.8
Beam diameter at exit, D_b (mm)	7.8	9.2

Table 3 Parameters of the PB

Parameter	Value
Resonant frequency, f (MHz)	2856
Quality factor, Q_0	1446
Coupling coefficient, β_c	1.27
Shunt impedance, Z_s ($M\Omega/m$)	2.33

loading effect, when the pulse current is 200 mA, the input power calculated using Eq. (10) is 6.6 kW. The maximum RF power assigned to the PB is 100 kW, which is adjusted using a waveguide phase shift attenuator that provides a maximum attenuation of 40 dB, ensuring that the power distribution is sufficient to meet the demand. Figure 4 shows the longitudinal distribution of the beam before and after the PB. According to the simulation results, the long pulse beam is bunched into bunches after passing through the PB, and the bunch interval is 350 ps.

3.2.2 Bunching-accelerating structure and accelerating structure

To achieve a high accelerating gradient and improve the accelerating efficiency, a $2\pi/3$ -mode traveling-wave accelerating structure is proposed. Typically, the objective for the beam is to attain high-energy levels within the accelerator as quickly as possible. The physical design requires the energy gain of the BA to reach 6.75 MeV without decreasing below 3.25 MeV in the AS. Therefore, the RF power allocated to the BA and AS is given by a ratio of approximately 2 to 1. To better capture and accelerate the beam in the low-energy section, the BA adopts β_ϕ cavities as an initial variable that matches the particle velocity to improve the transmission efficiency. The particle velocity is approximately equal to the speed of light after the BA; therefore, the AS adopts cavities with the phase velocity of light.

To satisfy the energy requirements, the energy gain in the BA and AS with the beam loading effect must be accurately calculated. The electric field formula and power balance in the traveling-wave cavity are given by Eqs. (11) and (12), respectively, whereas the longitudinal motion is expressed by Eqs. (13) and (14), where E_0 denotes the

accelerating gradient established in the traveling-wave cavity, α denotes the attenuation constant of the cavity, φ denotes the phase of the traveling-wave field, λ denotes the wavelength, and β denotes the ratio of the particle velocity to the speed of light [24, 25].

$$E_0(z) = \sqrt{2\alpha(z)Z_s P_{in}(z)}, \tag{11}$$

$$\frac{dp}{dz} = -2\alpha P - I_b E_0(z), \tag{12}$$

$$\frac{d\gamma}{dz} = \frac{eE_0}{m_0 c^2} \cos \varphi, \tag{13}$$

$$\frac{d\varphi}{dz} = \frac{2\pi}{\lambda} \left(\frac{1}{\beta_\phi} - \frac{1}{\beta} \right). \tag{14}$$

The Superfish program [26] was used to calculate the geometry, shunt impedance, quality factor, and attenuation constant of the cavity at various phase velocities. To achieve an energy gain greater than 6.75 MeV and a small energy spread, the phase velocity cavity of the BA was designed and optimized. The BA consists of one cavity each with phase velocities of 0.5, 0.68, 0.85, and 0.95, and 30 cavities with a phase velocity of 1. The AS consists of 31 cavities with a phase velocity of 1. The beam energy can reach 6.8 MeV at the exit of the BA with a pulse current of 200 mA and an input power of 2.6 MW. The dynamic calculation results are presented in Fig. 5. The beam energy can reach 10.2 MeV at the exit of the AS with a pulse current of 200 mA and an input power of 1.3 MW. Considering the uncertainty of equipment processing and changes in the operating status, approximately 3 MW and 1.5 MW of power are allocated to the BA and AS, respectively, with a margin of approximately

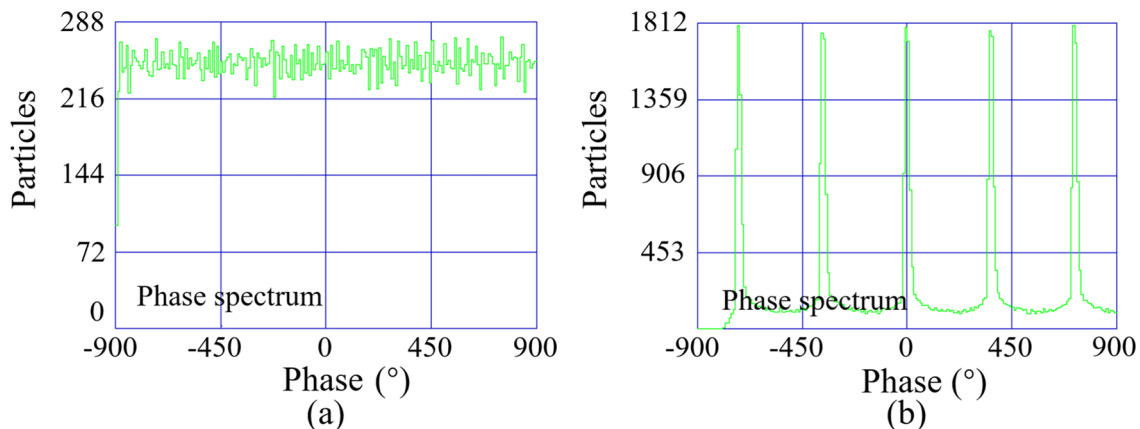


Fig. 4 (Color online) Beam distribution before (a) and after bunching (b). The vertical coordinate indicates the number of macroparticles whereas the horizontal coordinate indicates the longitudinal phase

Fig. 5 (Color online) Energy gain and phase width along the BA with a pulse of 200 mA and input power of 2.6 MW

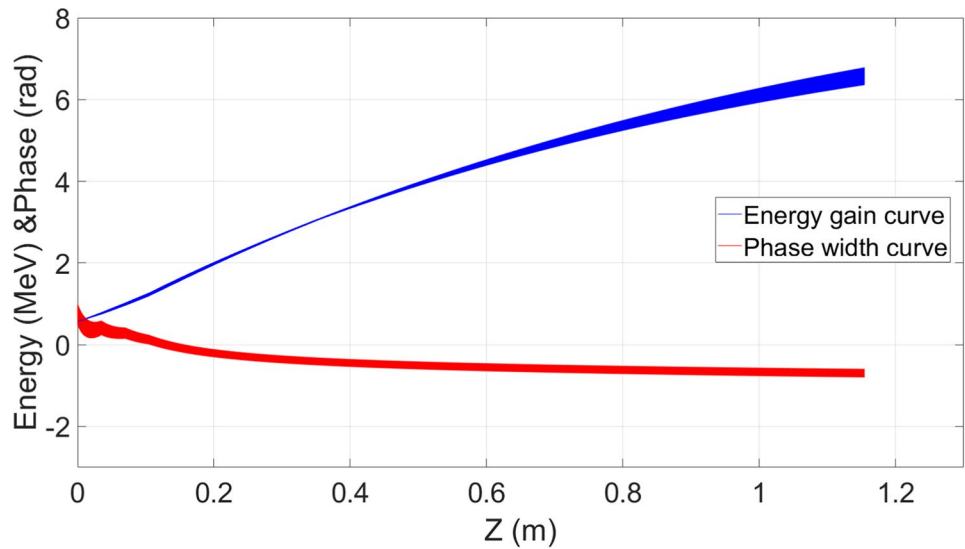


Table 4 Traveling-wave cavity parameters

Parameter	BA	AS
RF frequency, f_{RF} (MHz)	2856	2856
Shunt impedance, Z_s (M Ω /m)	31.8–65.6	60.8–65.6
Quality factor, Q_0	10,360–14,054	14,055–14,025
γ_g/c	0.01298–0.0073	0.0132–0.0073
Attenuation constant, α (Np/m)	0.182–0.324	0.179–0.323
Filling time, t_F (ns)	418	403
β_ϕ	0.5, 0.68, 0.85	1 (31 cells)
RF power, P (MW)	3	1.5

Table 5 Parameters of solenoid magnet

Parameter	SOL-I	SOL-II	SOL-III
Quantity	3	1	8
Length, L_{sol} (mm)	80	80	120
Inner diameter, D_b (mm)	90	160	235
Magnetic field, B (Gs)	200	300	800

10%. Table 4 shows the design parameters for the BA and AS.

3.2.3 Solenoid magnetic field

To minimize beam loss and save longitudinal space, a solenoid magnetic field was used to constrain the beam transverse size. Based on the physical design and related component specifications, three types of solenoid magnets, described in Table 5, are required. The focused magnetic field was designed to control the beam envelope by adjusting

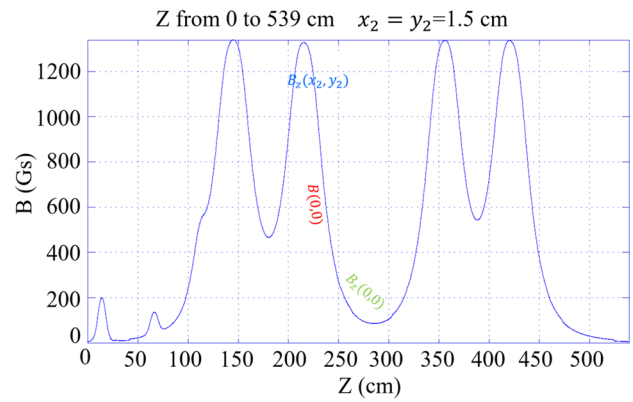


Fig. 6 (Color online) Solenoid magnetic field distribution

the solenoid position and magnetic field strength, as shown in Fig. 6.

3.2.4 Beam dynamics

The beam dynamics was calculated using PARMELA [27] assuming a pulse current of 200 mA as an example. The initial number of macroparticles was set to 50,000 in the simulation, starting from the electron gun exit. Figure 7 shows the transverse envelope of the beam in the bunching-accelerating section. To minimize the beam loss at the entrance of the AS and ensure the reliability of the accelerating structure, a collimator, referred to as COL1, was introduced at the entrance of the AS.

According to the simulation results, the beam energy reaches 10.3 MeV at the exit of the AS with a transmission efficiency of 88.6%, as shown in Fig. 8a. In the figure, ‘ngood’ represents the number of macro particles. The

Fig. 7 (Color online) Beam transverse envelope along the bunching-accelerating section

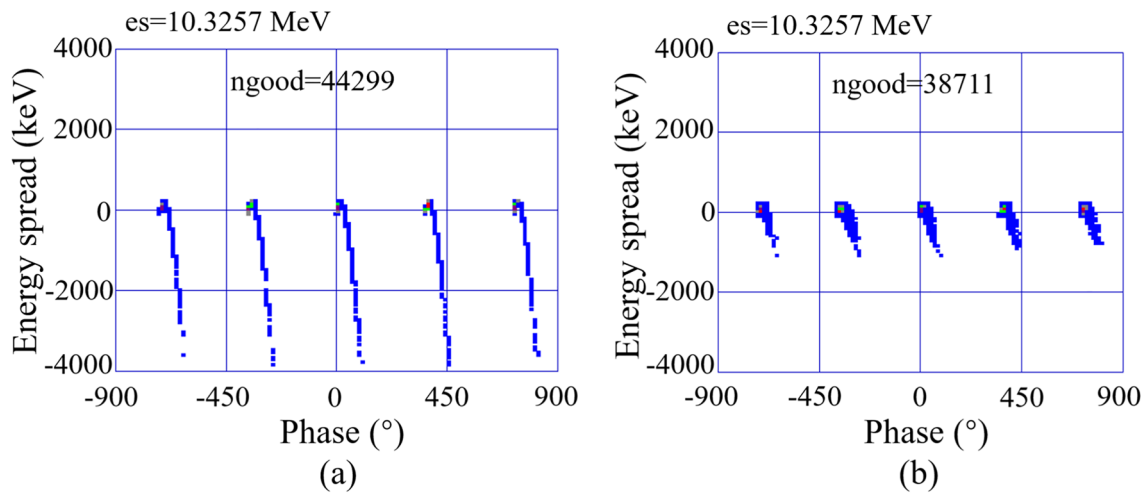
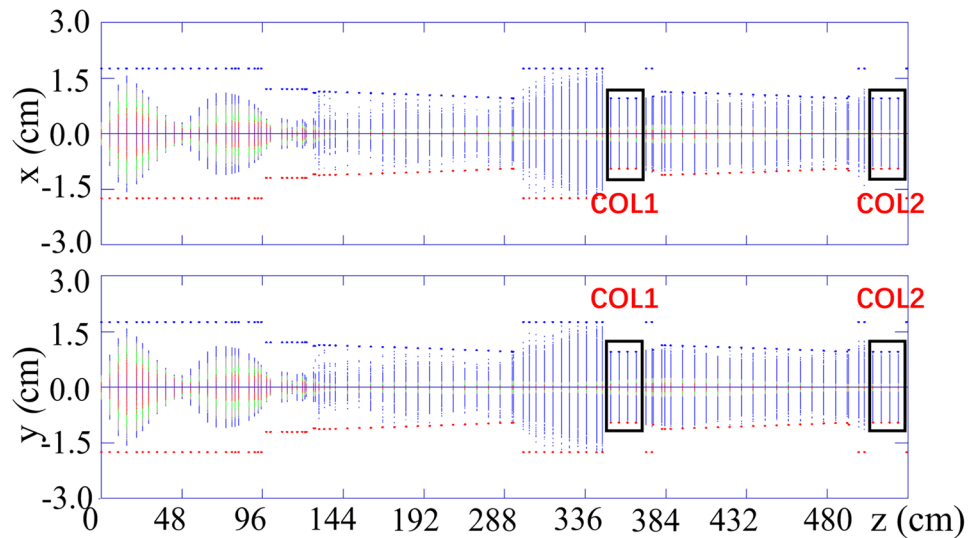


Fig. 8 (Color online) Beam energy spectrum at the exit of the AS (a) and energy analysis station (b)

beam has a long momentum tail with a maximum energy deviation exceeding 3 MeV. These particles with a large momentum spread are lost in the subsequent transport line. To localize the beam loss and protect the critical beam diagnostic equipment, a collimator named COL2 was incorporated at the exit of the AS. The energy analysis station includes the AM, PR4, and other components to measure the energy and energy spread. The deflection angle of the AM is 25°, and the deflection radius is 0.45 m. The energy distribution of the particles in PR4 is shown in Fig. 8b, which indicates that the energy deviation is within 1 MeV.

Adjusting the phase of the traveling-wave field allows the beam to complete the accelerating or decelerating process in the AS. The transmission efficiency, energy spread, and emittance for different energies of the beam and two operating pulse currents are shown in Fig. 9.

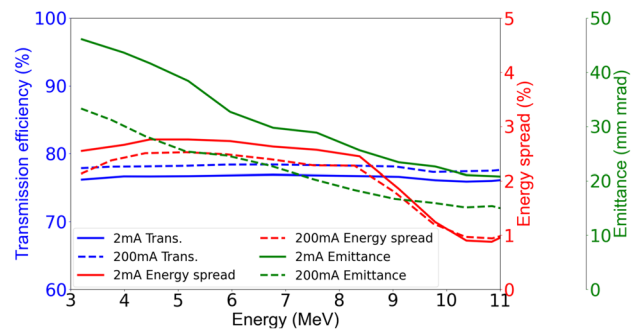


Fig. 9 (Color online) Results of beam optics design

Based on the simulation results, the energy can be adjusted from 3.5 to 10 MeV for both pulse currents, and the final transmission efficiency is greater than 75%. The energy spread is less than 3% at 3.5 MeV and approximately 1% at the energy analysis station for 10 MeV. Because of the optimization of the electron gun at a pulse current of 200 mA, the emittance of the 2 mA beam is greater than that of the beam with a pulse current of 200 mA. The emittance for both pulse currents is less than $30 \text{ mm} \cdot \text{mrad}$ at 10 MeV.

3.3 Scanning transport line

The scanning transport line includes beam diagnostic equipment, quadrupoles, correction magnets, a kicker, and an SM. The beam diagnostic equipment measures the energy, energy spread, and pulse current. The combination of quadrupoles constrains the transverse envelope of the beam on the transport line, improving its transmission efficiency in vacuum pipes and meeting the irradiation requirements of a small horizontal size and large vertical size. The combination of a kicker and an SM achieves an irradiated area with a scanning rate of 100 Hz, ensuring a uniformity higher than 90% at Targets A (0.04 m^2) and B (1 m^2).

According to the requirements of the beam irradiation area and uniformity, the scanning system adopts a scheme of single-direction beam expansion and two-direction scanning. The pulsed beam has a period of 2 ms, and the beam pulse width is $15 \mu\text{s}$. The scanning rate is 100 Hz. A kicker with linearly varying electromagnetic field is employed for rapid and continuous scanning in the horizontal direction. For this electromagnetic field, each bunch in the pulsed beam is deflected to a different position and evenly distributed in the horizontal direction of the target. The duration of the linearly varying field exceeds $15 \mu\text{s}$. Subsequently, the SM is used for vertical deflection in five steps, with the flat-top time of the magnetic field exceeding $15 \mu\text{s}$ for each step. The steps and time structure of the beam scanning are shown in Fig. 10.

After passing through the BA and AS, the beam is bunched into multiple bunches, with an interval of one RF period between the bunches. The beam pulse width is $15 \mu\text{s}$, which results in approximately 42,857 bunches. In the horizontal direction of the target, the beam is distributed over more than 40,000 bunches, making it easy to achieve uniformity. Five pulsed beams are superimposed vertically to achieve a wide irradiation range. This requires the magnetic field of the quadrupoles to be adjusted to expand the beam size in the vertical direction. Different beam sizes can be controlled for different targets to satisfy different irradiation range requirements. To measure uniformity, the targets were divided equally into a 5×5 grid, and an FC was placed at each grid point to form an FC array. The pulse current of each FC was measured, and the beam intensity uniformity was calculated using Eqs. (3) and (4).

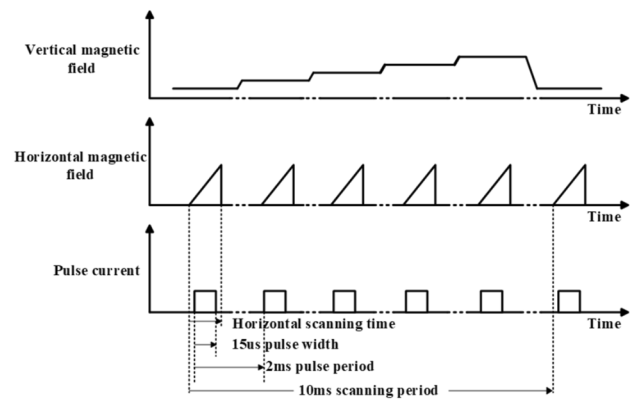


Fig. 10 (Color online) Beam scanning and time structure

The beam superposition described in Sect. 2.1 was simulated using a Gaussian distribution. However, the real distribution differs from this Gaussian distribution. In addition, the deflection of the beam with the energy spread by the scanning system produces a dispersion effect, leading to an increase in the transverse beam size. Therefore, ELEGANT [28] was used to simulate the dynamics. After matching the beam size, the beam intensity uniformity and beam percentage in the vertical direction of Target A were obtained by varying the magnetic field of the SM to deflect the beams to different positions μ_y , as shown in Fig. 11.

To meet the irradiation beam requirement and maximize the beam power, we selected a target area where the uniformity was higher than 90%, and the beam percentage was greater than 70%, as indicated by the boxed area in Fig. 11. When the beam percentage was between 70% and 72%, the maximum variation in uniformity was less than 0.3%. Taking into account redundancy and parameter sensitivity, we selected the point with a 72% percentage, as shown in Fig. 11. The irradiation area and normalized beam density of the two targets are shown in Fig. 12. The uniformity was 94.5%, and the beam percentage was 72.3% for Target A, whereas the uniformity was 94.1%, and the beam percentage was 72.2% for Target B.

Owing to the long distance between the SM and the targets, even a small change in the fields generated by the kicker and SM can cause a significant change in the position of the beam on the target. The results of the field error analysis for different targets are shown in Fig. 13. When the field of the kicker or SM is less than the design value and gradually decreases, the uniformity decreases quickly. Conversely, when the field is greater than the design value and gradually increases, the uniformity increases slowly, whereas the beam percentage decreases rapidly. For the kicker, the uniformity on Targets A and B is not satisfied when the error values exceed -5.9% and -5.3% , respectively. For the SM, the uniformity of both Targets A and B is better

Fig. 11 (Color online) Relationship between uniformity and beam percentage (vertical direction)

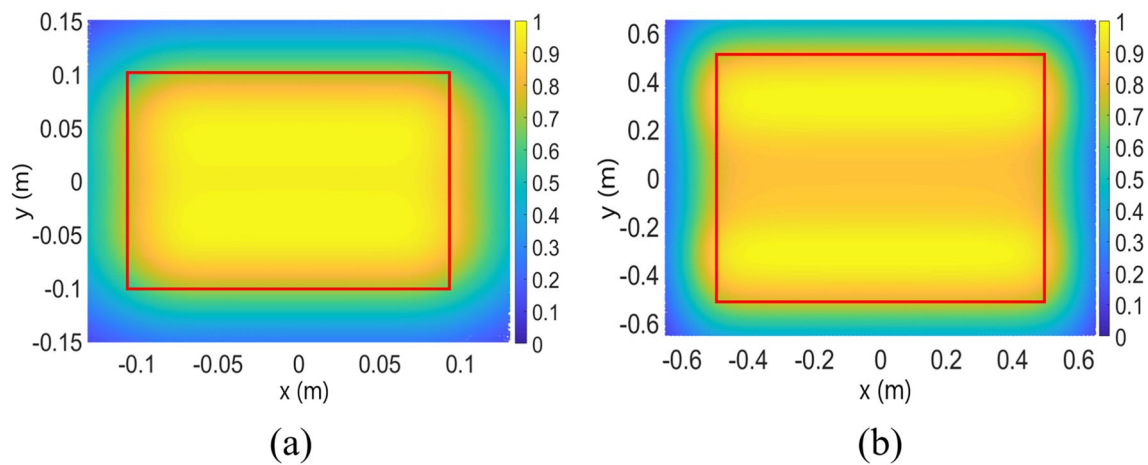
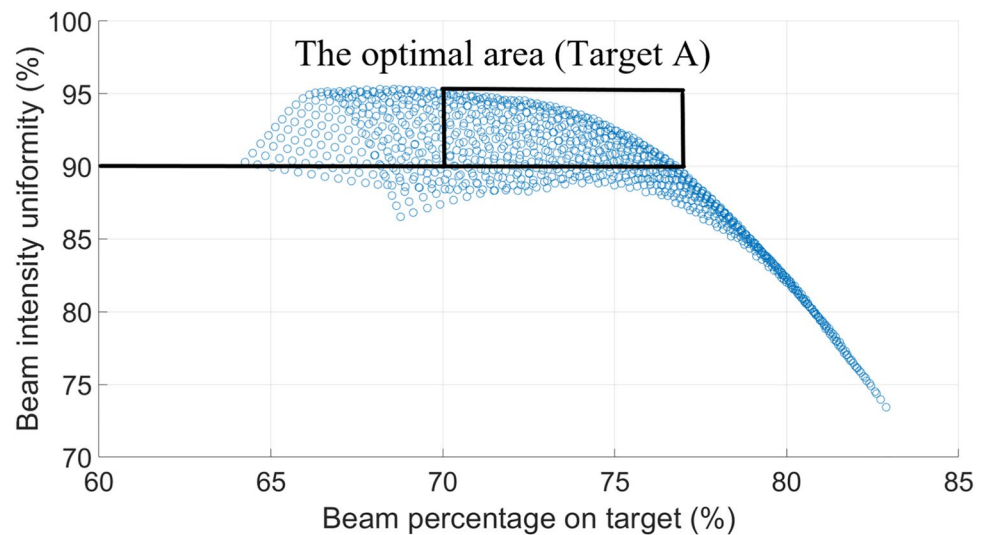


Fig. 12 (Color online) Results of the irradiation area and beam intensity at different targets: **a** Target A and **b** Target B

than 90% when the error value is within $\pm 10\%$. According to the aforementioned analysis, when the field error is within $\pm 5\%$, the uniformity can meet the requirements.

In the event of a failure in either the kicker or SM, the uniformity is not adequate. Furthermore, because the kicker and SM are separated by a titanium window, the failure of the kicker could result in an increase in the beam power density as it passes through the titanium window. Hence, it is essential to assess whether a titanium window is at risk of overheating and potential damage in the event of a kicker failure. For this analysis, Target A with a small beam size was selected for calculation.

When an electron beam with energy exceeding 0.5 MeV passes through the titanium window, the energy loss is proportional to the thickness of the titanium window, and its value is 640 keV/mm [29]. The titanium window thickness

is 0.04 mm; therefore, the energy loss is 25.6 keV, equating a power deposition of 25.6 W. The density distributions of the power deposition on titanium windows under kicker failure and normal operating conditions are shown in Fig. 14. The titanium window is air-cooled, with a convective heat transfer coefficient of $61 \text{ W}/(\text{m}^2 \cdot ^\circ\text{C})$. According to the conducted simulation, the maximum temperature at the center of the titanium window is $585 \text{ }^\circ\text{C}$ when the kicker fails and $425 \text{ }^\circ\text{C}$ during normal operation. Both values are significantly below the melting point of titanium, which is $1668 \text{ }^\circ\text{C}$. In both scenarios, the connection point between the titanium window and rubber remained at room temperature. Thus, in the event of a kicker failure, although uniformity may not be achieved, it does not pose a safety concern for the accelerator.

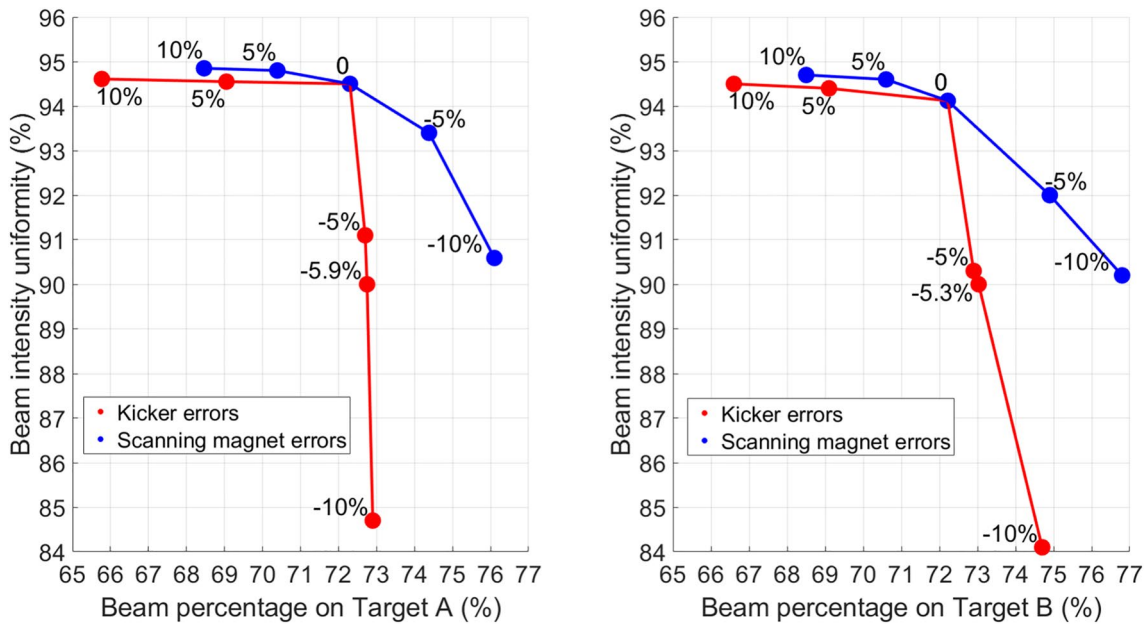
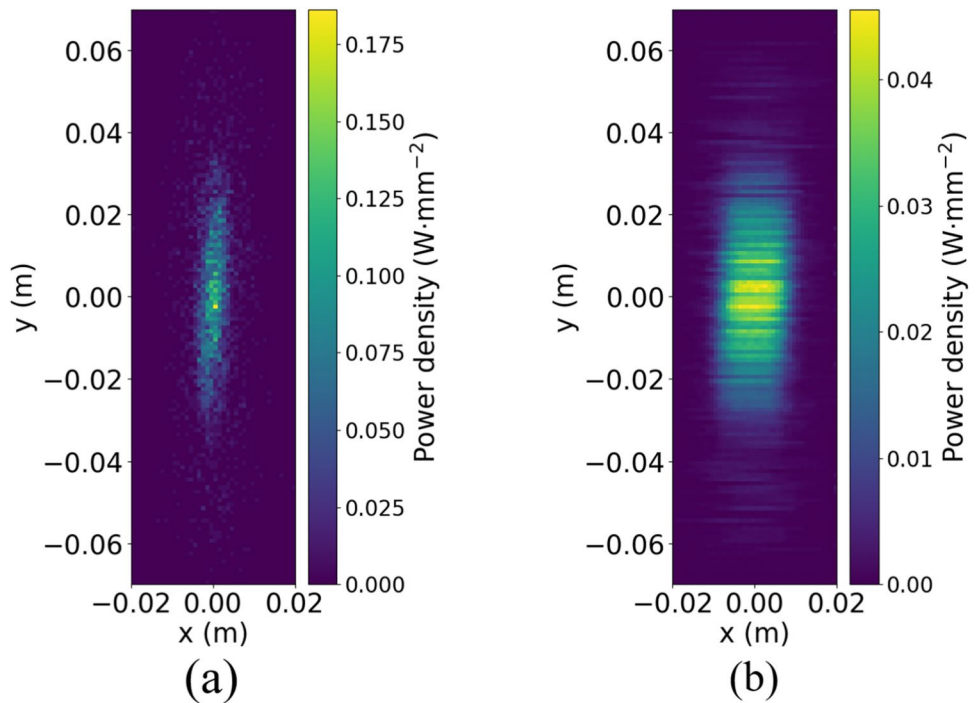


Fig. 13 (Color online) Tolerance on magnet errors for different targets: a Target A and b Target B

Fig. 14 (Color online) Density distribution of power deposition on the titanium window: a kicker failure and b kicker normal operation



3.4 Ambient magnetic field influence

Considering the effects of the geomagnetic field, surrounding facilities, and buildings at the site, there will be an ambient magnetic field around the linac. According to the existing scheme, electrons are transported through free space over a considerable distance. The beam may shift in the transverse

direction under the influence of this magnetic field and subsequently deviate from the center of the orbit. The measured transverse components of the ambient magnetic field, B_x , B_y , and B_z , are 0.33 Gs, 0.07 Gs, and -0.36 Gs, respectively. According to the simulation results, the beam offset in the horizontal direction is -0.08 mm for Target A and approximately 4.1 mm for Target B. In the vertical direction, the

beam offset is -27 mm for Target A and -66 mm for Target B. The influence of the ambient magnetic field is significant. To mitigate this effect, correction magnets were added in the middle of the quadrupoles. The beam trajectories with and without correction are shown in Fig. 15.

4 Hardware considerations and preliminary linac commissioning

To ensure the stable operation of the linac, hardware plays an important role in complementing the physics design. This section presents some design considerations for the hardware such as water cooling requirements and cavity materials of the bunching-accelerating section. The preliminary beam-commissioning results of the accelerator are presented.

4.1 Water cooling requirements

Owing to the high average beam current of this accelerator, the beam power is very high, reaching 10 kW, and beam losses can cause localized heating. To ensure the stable operation of the accelerator, water cooling must be added to areas with beam losses. The main locations of beam and power losses are shown in Fig. 16. The main power losses at different positions are as follows: COL1 at approximately 0.13 kW, COL2 at 0.06 kW, vacuum pipes for Q1 and Q2 at 0.17 kW, vacuum pipes for AM at 0.3 kW, and vacuum pipes

for Q3 and Q4 at 0.5 kW. Water cooling has been added at the aforementioned locations.

4.2 Cavity materials

According to the physical design, the cavity voltage requirement for the PB is relatively low. To achieve low sensitivity to frequency variations and high operational stability, we aimed to achieve a relatively low-quality factor for the PB [22]. Therefore, we opted for a design using stainless steel, while still using oxygen-free copper as the nose cone. Oxygen-free copper has excellent machinability and high electrical and thermal conductivities. The cavities of the BA and AS use oxygen-free copper material to meet high-precision requirements during processing and ensure stable electromagnetic wave propagation. Additionally, the BA and AS integrate a water jacket for enhanced water cooling to meet the heat dissipation requirements of the accelerating structure during operation.

4.3 Preliminary beam commissioning

The installation of the linac has been completed, as shown in Fig. 17. The commissioning stage is currently underway. Table 6 lists the preliminary commissioning results, indicating that the beam energy, energy spread, pulse current and width, irradiation area, and uniformity meet the specified parameters. Currently, the linac can operate at

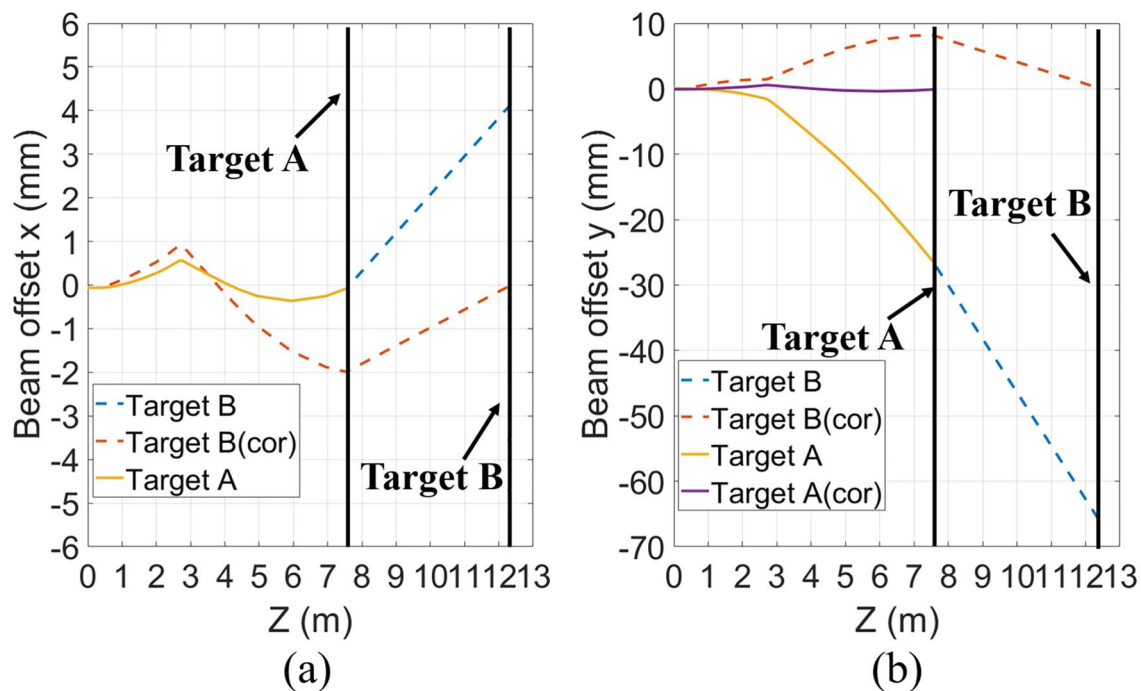


Fig. 15 (Color online) Beam offset in different directions: **a** x -direction and **b** y -direction

Fig. 16 (Color online) Distribution of power loss location

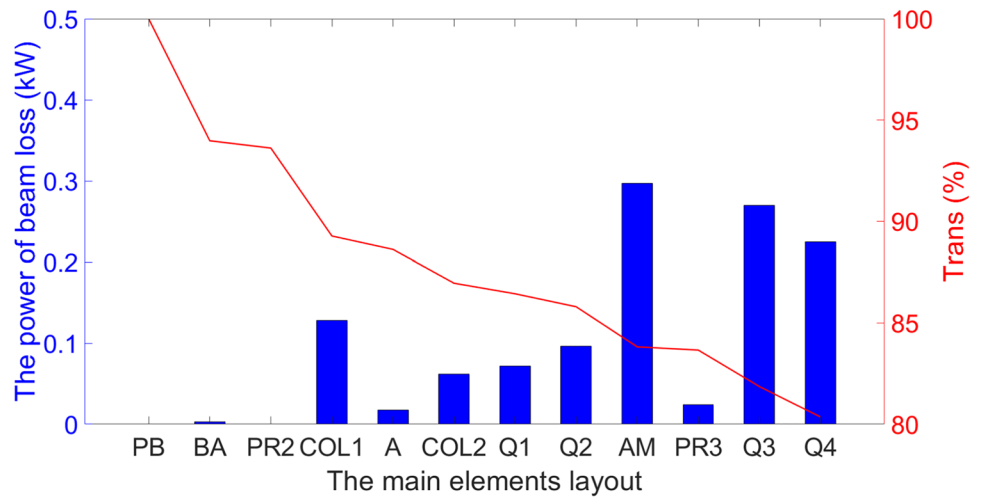


Fig. 17 (Color online) 10 MeV electron linac

Table 6 Results of 10 MeV electron linac commissioning

Parameter	Requirement value	Test value
Beam energy, W_0 (MeV)	3.5–10	10.08
Energy spread, δ (%)	≤ 2.5 (10 MeV)	1.08
Pulse current, i_b (mA)	1.33–133.3	1–135.2
Pulse width, t (μ s)	15	15
Irradiation area, A_s (m^2)	0.2×0.2 (Target A)	0.2×0.2 (Target A)
	1×1 (Target B)	1×1 (Target B)
Beam intensity uniformity, S (%)	≥ 90	91.1 (Target A)
		90.7 (Target B)

a repetition rate of 250 Hz with all systems functioning normally. The next steps involve gradually increasing the repetition rate and optimizing the beam parameters.

5 Conclusion

This paper presents the parameters of a 10 MeV/10 kW electron linac for space environment simulation, along with a detailed physical design. The EGUN code was used to simulate the thermal cathode electron gun. A two-stage acceleration mechanism is proposed to meet the beam energy requirement over a wide range, considering the beam loading effect. PARMELA was used for relevant beam dynamic simulations. A method using a combination of a kicker and an SM is proposed to achieve a 100 Hz scanning rate. This method provides beams with a high scanning rate, large irradiation area, and high uniformity. Tolerance analyses for magnet errors and failure, as well as the influence of ambient magnetic fields on the beam transverse deviation, were considered and simulated using ELEGANT. All the simulation results indicate that the physical design can meet these requirements. To ensure the stable operation of the linac, this study also examined the materials of the cavities and water cooling requirements. Finally, the commissioning progress and preliminary beam test results are presented. Beam commissioning and optimization are currently underway. The development of this linac provides a solid research foundation for researchers engaged in the field of high scanning rate electron linacs.

Acknowledgements The authors would like to express their gratitude to Dr. Hai-Jing Wang for assistance with the thermal analysis of the titanium window and also thank their colleagues for their valuable suggestions and comments.

Author Contributions All authors contributed to the study conception and design. Material preparation, data collection, and analysis were performed by SZ, CM, Z-SZ, XH, J-RZ, MI, Z-DZ, B-WB, and Y-LC. The first draft of the manuscript was written by Shu Zhang, and all authors commented on the previous versions of the manuscript. All authors read and approved the final manuscript.

Data Availability The data that support the findings of this study are openly available in Science Data Bank at <https://cstr.cn/31253.11.sciencedb.j00186.00098> and <https://doi.org/10.57760/sciencedb.j00186.00098>.

Declarations

Conflict of interest The authors declare that they have no conflict of interest.

References

- J.J. Zhao, Z.S. Yi, *Particle Accelerator Technology* (Higher Education Press, Beijing, 2006). (in Chinese)
- Y. Ha, F. Wang, H. Shi et al., Application and characteristics of food irradiation by electron beam. *J. Nucl. Agric. Sci.* **21**, 61–64 (2007). <https://doi.org/10.11869/hnxb.2007.01.0061>. (in Chinese)
- S. Zhang, J.R. Zhang, Z.S. Zhou et al., *Physics design of a 10 MeV High scanning frequency irradiation electron linear accelerator*, in *Proceedings of IPAC 2022, Bangkok, Thailand* (2022), pp. 2476–2478. <https://doi.org/10.18429/JACoW-IPAC2022-THPOS T017>
- W. Li, M.K. Hudson, Earth's Van Allen radiation belts: from discovery to the Van Allen probes era. *J. Geophys. Res.-Space.* **124**, 8319–8351 (2019). <https://doi.org/10.1029/2018JA025940>
- C.Q. Wang, Y.H. Xiang, J.H. Li et al., Design of beam homogenization for ground simulation of space electron environment. *Nucl. Tech.* **43**, 120201 (2020). <https://doi.org/10.11889/j.0253-3219.2020.hjs.43.120201>. (in Chinese)
- Y. Kamino, 10MeV 25kW industrial electron Linac. *Radiat. Phys. Chem.* **52**, 469–473 (1998). [https://doi.org/10.1016/S0969-806X\(98\)00053-X](https://doi.org/10.1016/S0969-806X(98)00053-X)
- Q.J. Lai, D.X. Xie, Y.Z. Zhu et al., NFZ-10 Industrial irradiation electron Linac. *High Power Laser Particle Beams* **10**, 305–308 (1998). (in Chinese)
- B. Von Przewoski, T. Rinckel, W. Manwaring et al., *Beam properties of the new radiation effects research stations at indiana university cyclotron facility*, in *2004 IEEE. Radiat. Effects. Atlanta, GA, USA* (2004), pp. 145–150. <https://doi.org/10.1109/REDW.2004.1352921>
- T. Furekawa, T. Inaniwa, S. Stao et al., Design study of a raster scanning system for moving target irradiation in heavy-ion radiotherapy. *Med. Phys.* **34**, 1085–1097 (2007). <https://doi.org/10.1118/1.2558213>
- Z. Guo, J.Y. Tang, Z. Yang et al., A novel structure of multipole field magnet and their applications in uniformizing beam spot at target. *Nucl. Instrum. Meth. A.* **691**, 97–108 (2012). <https://doi.org/10.1016/j.nima.2012.06.048>
- B.L. Jia, L.H. Ouyang, Z.T. Zhao, Simulation of an octupole scanning magnet for spot scanning in proton therapy. *IEEE. Trans. Appl. Supercon.* **28**, 4400304 (2017). <https://doi.org/10.1109/TASC.2017.2773828>
- B. Sherrill, J. Kashy, E. Kashy et al., Use of multipole magnetic fields for making uniform irradiations. *Nucl. Instrum. Meth. B.* **40–41**, 1004–1007 (1989). [https://doi.org/10.1016/0168-583X\(89\)90527-2](https://doi.org/10.1016/0168-583X(89)90527-2)
- J.Y. Tang, H.H. Li, S.Z. An et al., Distribution transformation by using step-like nonlinear magnets. *Nucl. Instrum. Meth. A.* **532**, 538–547 (2004). <https://doi.org/10.1016/j.nima.2004.05.124>
- D. Barlow, R. Shafer, R. Martinez, *Magnetic design and measurement of nonlinear multipole magnets for the APT beam expander system*, in *Proceedings of PAC, et al., Vancouver. Canada 1997* (1997), pp. 3309–3311. <https://doi.org/10.1109/PAC.1997.753191>
- R.J. Shi, *An Introduction to Electron Accelerators and Industrial Applications* (China Metrology Publishing House, Beijing, 2012). (in Chinese)
- J.B. Zhu, H. Shi, B.W. Bai et al., Study of a 560-mm-long strip-line kicker for HIT 10 MeV electron accelerator. *Radiat. Detect. Technol. Methods* **5**, 373–378 (2021). <https://doi.org/10.1007/s41605-021-00256-7>
- R. Garoby, *Beam Loading in RF Cavities* (Springer, Berlin, 1992). https://doi.org/10.1007/3-540-55250-2_42
- R. Corsini, H. Braun, G. Carron et al., *First full beam loading operation with the CTF3 Linac*, in *Proceedings of EPAC 2004, Lucerne, Switzerland* (2004), pp. 39–41. <https://doi.org/10.2172/833095>
- A. Mostacci, M. Bellaveglia, E. Chiadroni et al., Chromatic effects in quadrupole scan emittance measurements. *Phys. Rev. Spec. Top AC.* **15**, 082802 (2012). <https://doi.org/10.1103/PhysRevSTAB.15.082802>
- W.B. Herrmannsfeldt, EGUN: an electron optics and gun design program (Stanford Linear Accelerator Center, Menlo Park, CA). <https://doi.org/10.2172/6711732>
- X. He, G.Y. Feng, J.D. Liu et al., An S-band variable waveguide power divider and combiner for high-vacuum and high-vacuum and high-power applications. *IEEE. Trans. Microw. Theory* **71**, 3761–3772 (2023). <https://doi.org/10.1109/TMTT.2023.3242343>
- X. He, M. Hou, F.L. Zhao et al., Design of a beam phase cavity and a waveguide coupled eccentric circle structure prebuncher in S-band. *High Power Laser Part. Beams* **27**, 250–253 (2015). <https://doi.org/10.1184/HPLPB201527.075102>
- S. Lai, K.K. Pant, Study of beam loading and its compensation in the compact ultrafast terahertz free-electron laser injector linac. *Rev. Sci. Instrum.* **85**, 123302 (2014). <https://doi.org/10.1063/1.4902563>
- T.P. Wangler, *RF linear Accelerators*, 2nd edn. Wiley-VCH Verlag GmbH & Co (KGaA, Weinheim) (2008)
- Y.J. Pei, *Fundamentals of Electron Linear Accelerator Design* (Science Press, Beijing, 2013). (in Chinese)
- J.H. Billen, L.M. Young, Superfish poisson, on PC compatibles, in *Proceedings of PAC, Washington. USA, 1993* (1993), pp. 790–792. <https://doi.org/10.1109/PAC.1993.308773>
- L. Young, J. Billen, *The particle tracking code PARMELA*, in *Proceedings of PAC 2003, Portland* (2003), pp. 3521–3523. <https://doi.org/10.1109/PAC.2003.1289968>
- M. Borland, *Elegant: A flexible SDDS-complaint code for accelerator simulation*, in *Proceedings of ICAP 2000, Dramstadt, Germany* (2000). <https://doi.org/10.2172/761286>
- X.H. He, L.B. Lin, D.X. Xiao et al., Cooling of electron beam extraction window. *At. Energy Sci. Technol.* **43**, 925–930 (2009). (in Chinese)

Springer Nature or its licensor (e.g. a society or other partner) holds exclusive rights to this article under a publishing agreement with the author(s) or other rightsholder(s); author self-archiving of the accepted manuscript version of this article is solely governed by the terms of such publishing agreement and applicable law.